the high affinity of carbon for certain metals (*11*), molten metal nanoparticles are able to act as catalytic sites for the uptake of carbon with subsequent carbon nanotube outgrowth (*12*).

Under continuing heating, we observed nanowire growth over the course of 10 min (Fig. 3). Movie S2, taken at a higher resolution, better shows the initial stages of growth at high temperature (*10*). The faceted end of the emerging wire indicates that the free end of the wire is solid during the growth process.

Because the walls of the microcrucible contain the ions that are consumed in the formation of the nanowire, as the nanowire grows it would be expected that the dimensions of the microcrucible itself would change, leading to alteration of the nanowire morphology. The continual evolution of the liquid-solid interface of the microcrucible is a dynamic process that leads to creep of the interface and the concomitant morphogenesis of nonclassical crystal structures. Changes in the structure of the microcrucible have been observed previously in the growth of BSCCO and Y123 whiskers at the microscale, with the resultant creation of single-crystal morphologies as unorthodox as bows and rings (*13*, *14*). In this work, microcrucible creep resulted in two distinct nanowire morphologies: (i) those that underwent growth in both length and width and (ii) those for which two nearby microcrucibles joined together to form wires with "stepped" ends. Figure 4 shows nanowires with stepped ends as a result of two microcrucibles joining together (Fig. 4, A and B), as well as the progression of a growing wire over the course of 5 min, which shows the walls of the microcrucible breaking down (Fig. 4, C and D). Because the nanowire in Fig. 4C is short and at high temperature, the molten material is able to wet the side edge of the nanowire as the microcrucible supporting it breaks down (allowing for a droplet of greater diameter), causing a rapid and uniform increase in width. Evidence of creep can also be seen in Fig. 1D, where the regions of the nanowire at the edges of the microcrucible are crystallographically distinct from those in the center. A degree of control of the liquid-solid interface is exhibited here, as the $BaCO_3$ nanoparticles are of low-size polydispersity (*15*) and therefore limit the type and amount of creep in the system and, consequently, the diversity of structural features in the nanowires.

In previous studies on the synthesis of quaternary oxide nanowires (*15*, *16*), nanowires grew with a tapered morphology and a VLS-like catalytic drop. The key difference in those studies was that carbon-rich precursors such as citrate and acetate were used in the syntheses; these substances tend to persist for longer under calcination (*17*, *18*) than do the nitrates used here (fig. S7). In turn, this leads to a lower-density matrix, enabling nanoparticles to leave the surface and act as catalytic sites on the leading edges of the outgrowing nanowires. This is followed by tapered growth as the nanoparticle is consumed, producing morphologies more reminiscent of a VLS process. The loss of nitrates at a lower cal-

cination temperature means that in this work, the matrix is denser at the point at which nanowire growth begins. We deduce that here the matrix is still porous and reticulated, but the higher density will therefore tend to entrap Ba-rich nanoparticles at the surface and lead to the microcrucible growth observed. It is likely that in previous reports where nitrate precursors were used to form the complex oxides of $La_3Ga_5SiO_{14}$ (*19*) and $La_{0.67}Sr_{0.33}MnO_3$ (*20*) via a porous matrix, the faceted-ended nanowires produced were also the result of a microcrucible mechanism.

Through judicious design of the synthetic protocol, we have demonstrated the direct observation of a microcrucible growth mechanism and confirmed that it is a viable method for the growth of complex oxide nanowires. The successful formation of nanowires is predicated on the presence of a catalytic nanoparticle and a porous matrix that enables migration of the former through the latter, leading to nanowire outgrowth at the surface. The uniform cross section arising from the microcrucible mechanism means that the nanowires produced in this way will have the same physical properties along their entire length, leading to more uniform current-carrying ability, ferroic behavior, and tensile strength for the future use of complex functional oxide nanowires in applications.

References and Notes

1. G. A. Ozin, *Nanochemistry—A Chemical Approach to Nanomaterials* (Royal Society of Chemistry, Cambridge, 2005).
2. K. Xu, J. R. Heath, *Nano Lett.* **8**, 3845–3849 (2008).
3. Z. L. Wang, *J. Phys. Condens. Matter* **16**, R829–R858 (2004).
4. J. D. Berrigan *et al.*, *Adv. Funct. Mater.* **21**, 1693–1700 (2011).
5. I. Matsubara *et al.*, *J. Cryst. Growth* **141**, 131–140 (1994).
6. P. Badica, K. Togano, *J. Mater. Res.* **20**, 3358–3367 (2005).
7. P. Badica, K. Togano, S. Awaji, K. Watanabe, H. Kumakura, *Supercond. Sci. Tech.* **19**, R81–R99 (2006).
8. C. Yang, Z. Zhong, C. M. Lieber, *Science* **310**, 1304–1307 (2005).
9. K. Nagashima, T. Yanagida, K. Oka, H. Tanaka, T. Kawai, *Appl. Phys. Lett.* **93**, 153103 (2008).
10. See supplementary materials on *Science* Online.
11. Y. Cao *et al.*, *Nano Lett.* **12**, 3783–3787 (2012).
12. A. Gorbunov, O. Jost, W. Pompe, A. Graff, *Carbon* **40**, 113–118 (2002).
13. P. Badica *et al.*, *Supercond. Sci. Tech.* **25**, 105003 (2012).
14. S. Cagliero *et al.*, *Supercond. Sci. Tech.* **25**, 125002 (2012).
15. Z. A. Schnepp, S. C. Wimbush, S. Mann, S. R. Hall, *Adv. Mater.* **20**, 1782–1786 (2008).
16. S. R. Hall, *Adv. Mater.* **18**, 487–490 (2006).
17. L. A. Chick *et al.*, *Mater. Lett.* **10**, 6–12 (1990).
18. H. C. Zeng, S. K. Tung, *Chem. Mater.* **8**, 2667–2672 (1996).
19. Z. Schnepp, J. Mitchells, S. Mann, S. R. Hall, *Chem. Commun.* **46**, 4887–4889 (2010).
20. Z. Schnepp, S. C. Wimbush, S. Mann, S. R. Hall, *CrystEngComm* **12**, 1410–1415 (2010).

Spatially Distributed Local Fields in the Hippocampus Encode Rat Position

Gautam Agarwal,[1] Ian H. Stevenson,[1]* Antal Berényi,[2,3] Kenji Mizuseki,[2]†
György Buzsáki,[2]†† Friedrich T. Sommer[1]††

Although neuronal spikes can be readily detected from extracellular recordings, synaptic and subthreshold activity remains undifferentiated within the local field potential (LFP). In the hippocampus, neurons discharge selectively when the rat is at certain locations, while LFPs at single anatomical sites exhibit no such place-tuning. Nonetheless, because the representation of position is sparse and distributed, we hypothesized that spatial information can be recovered from multiple-site LFP recordings. Using high-density sampling of LFP and computational methods, we show that the spatiotemporal structure of the theta rhythm can encode position as robustly as neuronal spiking populations. Because our approach exploits the rhythmicity and sparse structure of neural activity, features found in many brain regions, it is useful as a general tool for discovering distributed LFP codes.

Two qualitatively different types of electric signals can be detected extracellularly, action potentials (spikes) and local field potentials (LFPs) (*1*–*5*), and these signals are regarded as complementary readouts of information about neuronal computation (*5*, *6*). As a rat moves through

its environment, hippocampal pyramidal cells spike at specific locations (place cells) (*7*). In contrast, the LFP maintains rhythmic (8 to 9 Hz) theta oscillations, independent of the rat's position (*8*, *9*). We hypothesized that the theta rhythm also contains information about the rat's position, since it is

primarily the place cell population whose membrane potential fluctuations give rise to the LFP ([10]).

Rats were implanted with 32-, 64-, or 256-site silicon probes in the hippocampus to monitor both LFP and unit firing (Fig. 1A) while they traversed a linear track (Fig. 1B), open field, or a T maze ([11]). When mapped onto electrode space, the theta rhythm showed spatiotemporal variations (Fig. 1A) that changed gradually over multiple cycles (movie S1). By analogy to radio communication, we defined the theta oscillation to be a carrier wave whose modulation contains information. This information was extracted from the theta rhythm using a demodulation operation (fig. S1).

[1]Redwood Center for Theoretical Neuroscience, University of California, Berkeley, Berkeley, CA 94720, USA. [2]The Neuroscience Institute, Center for Neural Science, New York University, School of Medicine, New York, NY 10016, USA. [3]Magyar Tudományos Akadémia-Szegedi Tudományegyetem (MTA-SZTE) Momentum Oscillatory Neuronal Networks Research Group, University of Szeged, Department of Physiology, Szeged, H-6720, Hungary.

*Present address: University of Connecticut, Department of Psychology, Storrs, CT 06269, USA.
†Present address: Allen Institute for Brain Science, Seattle, WA 98103, USA.
††Corresponding author. E-mail: fsommer@berkeley.edu (F.T.S.); gyorgy.buzsaki@nyumc.org (G.B.)

First, the theta-band-filtered oscillatory activity of each electrode was converted to a complex-valued signal, representing its instantaneous phase and amplitude (Fig. 1D). The carrier signal, identified by principal component analysis, was highly coherent across electrodes (Fig. 1D, lower trace). The demodulation operation then removed the phase of the theta carrier from each electrode, resulting in a spatiotemporal pattern of relative phase and amplitude that covaried smoothly (Fig. 1, E and F) with the rat's position.

The position of the rat during navigation was estimated from the demodulated LFP (Fig. 2 and fig. S2) and compared to spike-based decoding ([1, 7, 12, 13]). Although the cross-validated accuracy of the two decoders was comparable [optimal linear estimator (OLE) median error 6.7 ± 0.2 cm (LFP) and 9.2 ± 0.2 cm (spiking)] (Fig. 2G and fig. S2), they had distinct velocity and position dependence (Fig. 2, B and D). Accurate decoding of the theta rhythm depended on demodulation, as well as preserving the high dimensionality of the signal, even though the variance of the multielectrode signal was largely concentrated in a low-dimensional subspace (Fig. 2C), visible in the strong correlations in the LFP recorded at differ-
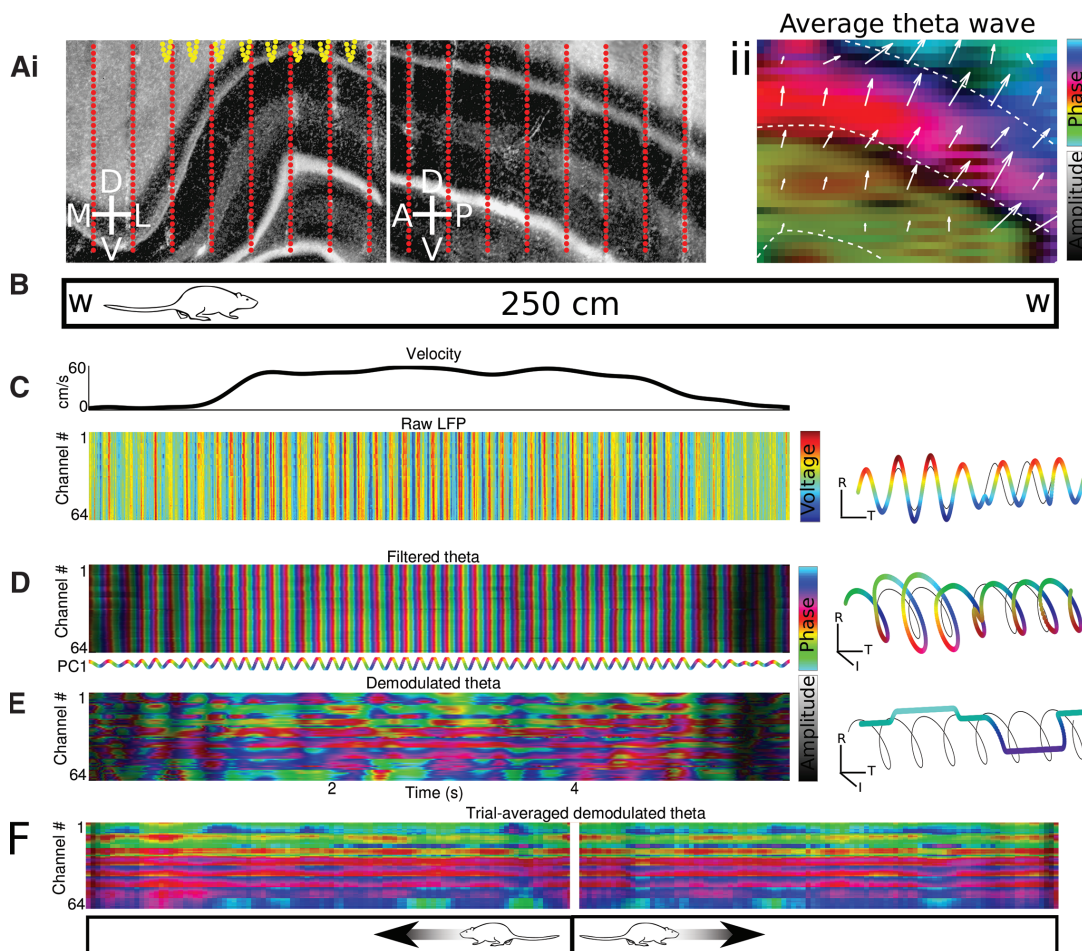
ent electrodes (Fig. 1, C and D). Whitening and Bayesian decoding methods further improved accuracy, especially in the open field (120 by 120 or 180 by 180 cm^2) (Fig. 2G).

Because position encoding is sparse, a theoretical result ([14]) based on compressed sensing ([15]) suggests that unsupervised learning can discover position-dependent sparse structure in the LFP without explicit knowledge of the rat's position. We tested this prediction by examining the evolving spatiotemporal distribution of the theta-filtered LFP using independent component analysis (ICA) ([16, 17]). A subset of the components [termed feature-tuned field potentials (FFPs)] showed selective activation at specific positions along one direction of motion (Fig. 3A and figs. S3 and S4) and comprised the major portion of the signal variance (53%, 69%, and 79% of total variance for $n = 3$ rats). When FFPs were projected back onto the anatomical space, they were distributed across the entire surface of the electrode array (Fig. 3B and movie S2).

We next asked whether the sparse structure of the broadband LFP (4 to 80 Hz) is also position dependent by training a convolutional sparse coding algorithm ([18]), which models signals as

Fig. 1. Recording space- and time-dependent variations in theta rhythm. (**Ai**) Arrangement of 64 (yellow) and 2 by 256 (red) electrode arrays implanted in the hippocampi of different rats. Left and right panels depict recordings along orthogonal axes: D/V, dorsoventral; A/P, anteroposterior; M/L, mediolateral. (**Aii**) Average spatial distribution of theta recorded by the electrode array in the right panel of (Ai) reveals systematic differences in the anatomical distribution of the theta rhythm. Arrows depict local phase gradients. (**B**) A rat runs across a 250-cm track to receive a water reward (w) at both ends. (**C** to **E**) (Left) LFP recorded during one run across the track. (Right) schematic of signal representation. Axes: T, time; R, real; I, imaginary. (C) Velocity of the rat (top) and the original, broadband signal (bottom), which shows a strong theta rhythm during running. (D) (Top) Filtering the signal with Morlet wavelet (5 to 11 Hz half-power cutoff) results in a complex-valued waveform with time-varying amplitude and phase. (Bottom) The first principal component (PC1) of the complex-valued signal, which tracks the global theta oscillation. (E) Demodulating the signal using PC1 as a carrier identifies modulations in amplitude and phase. (**F**) Averaging the demodulated signal over multiple runs reveals that its variations depend systematically on the rat's position. For (E) and (F), phase is scaled by a factor of 16 to emphasize time-varying structure.

a sparse superposition of spatiotemporal features. Despite differences in the analysis method and training data, the broadband components activated at single positions were spaced along the whole track, similar to the theta-band components (Fig. 3D and fig. S5). Each broadband feature exhibited the sawtooth waveform characteristic of hippocampal theta, with unique spatial variations in attributes such as onset and peak time (Fig 3C). Broadband features, similar to theta-band FFPs, remained largely silent outside a small range of preferred positions, each activating briefly at theta frequency (Fig. 3D).

The entire population of FFPs in a given session uniformly tiled the linear track (Fig. 4A). The phase of each demodulated FFP showed progressive advancement as the rat traversed the corresponding place field (Fig. 4A), reminiscent of the theta-phase precession of place cell spikes (19), and suggesting that the theta-rhythm arises largely from a population of phase-precessing neurons (10). The

distribution of the place fields of pyramidal cells was more irregular than that of the FFPs (Fig. 4B and fig. S6), consistent with the performance of the corresponding decoders (Fig. 2). Unlike FFPs, pyramidal cells had multiple place fields in one or both directions of travel, leading to distinct pairwise activity profiles of the populations (Fig. 4C and fig. S6). We also examined FFPs as the rat performed a spatial alternation memory task (20) in a T maze with a 10-s delay period in a large waiting area (Fig. 4D). Recordings from two 256-electrode arrays (11) contained ~50 FFPs that together covered the entire maze (Fig. 4D). About half of all FFPs densely tiled the two-dimensional (2D) waiting area (Fig. 4D). Most 2D place fields occupied largely similar positions independent of whether the rat came from a leftward or rightward journey (fig. S7). Accurate LFP decoding and identification of FFPs could also be performed on recording sites within the dendritic layers (fig. S8), excluding somatic layers where spikes were detected.

To understand how properties of FFPs relate to the activity of the underlying neuronal population, a simulation was constructed in which the LFP was modeled as the superimposed activity generated by numerous place-modulated synaptic inputs (fig. S9). Although individual electrodes showed weak place-tuning, their collective activity could nonetheless be decoded. Furthermore, ICA identified a large number of learned FFPs tuned to very specific locations of the track, consistent with theory (fig. S10) (14). However, as the trial-by-trial variability of neuronal activity was increased, ICA identified a decreasing number of FFPs. For noisy populations, FFP width increased in proportion to, but never exceeded, the tuning width of the underlying population's place fields.

We demonstrated that the rat's location is encoded by spatial variations of the hippocampal LFP. An often-assumed limitation of the LFP is that each electrode subsamples (pools) the activity of a large population of neurons. In topographically
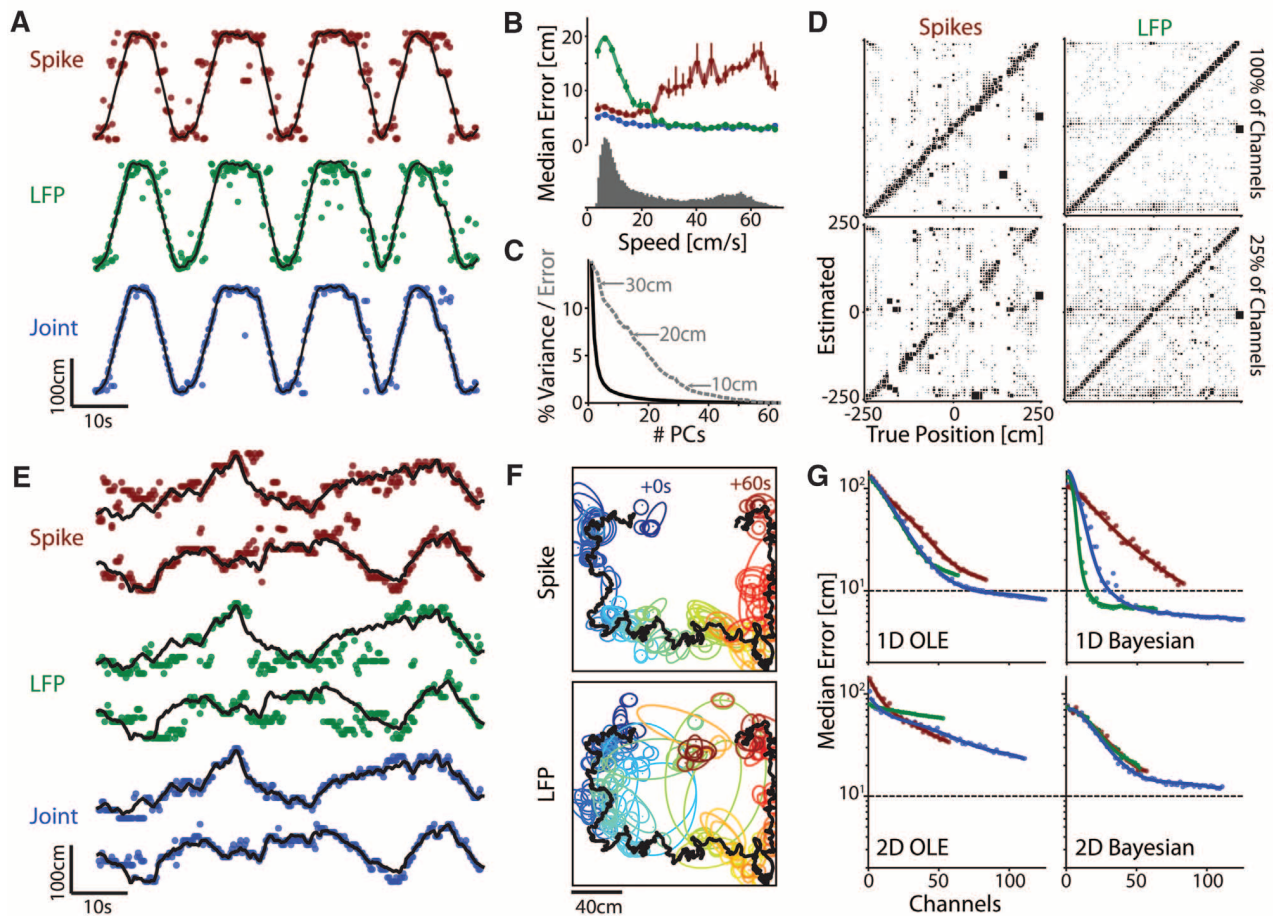

Fig. 2. Decoding of position by demodulated LFP and spikes. (**A**) Decoding of rat position on a linear track by LFP and spikes. Lines indicate actual trajectory, while dots indicate OLE estimate of position (*y* axis) at each time point (*x* axis). (**B**) LFP-based decoder performs best at high velocities, unlike spike-based decoder. The lower histogram shows the time spent at different speeds. (**C**) Variance is largely explained by PC1 (~85% of total variance, falling outside of plotted range), and accurate, cross-validated decoding depends on a large number of PC dimensions. (**D**) Histogram of decoder predictions; dark squares indicate high-probability events. Decoders trained on subsets of LFP channels (right) degrade uniformly, whereas those trained on spikes from subsets of neurons (left) degrade in a patchy manner. (**E**) Decoding of rat position in a 2D open field using a Bayesian filter-based decoder. Lines indicate actual trajectory in *x* and *y* coordinates; dots indicate decoder estimates. (**F**) Bird's eye view of actual (black) and estimated (color) position at different time points. Ellipses indicate ~1 SD confidence regions. (**G**) Median error of decoders as a function of the number of (random) channels used. Data is from rat ec014, with 64 electrodes straddling the cornu ammonis 1 (CA1) pyramidal layer. Identical color codes are used for (A), (B), (E), and (G).

Fig. 3. Sparse decompositions of oscillatory features in multielectrode data. (**A**) ICA of the signal reveals components, termed FFPs, that activate selectively at particular locations. (**B**) Each FFP exhibits a unique phase-amplitude relationship across the recorded area. For display purposes, FFPs are mean-subtracted to reveal differences (see supplementary materials). (**C**) Sparse decomposition of the broadband signal (4 to 80 Hz) reveals components that activate at corresponding locations and have distinctive broadband structure, consisting of diverse onsets and peaks. Individual traces are colored according to their corresponding electrodes in (B). (**D**) Broadband sparse components activate sequentially on the track, also exhibiting theta periodicity; components that activate in the reverse direction (black lines) remain silent. (Inset) Mean power spectrum of component activations. Data was recorded by a 64-electrode array implanted in CA1.
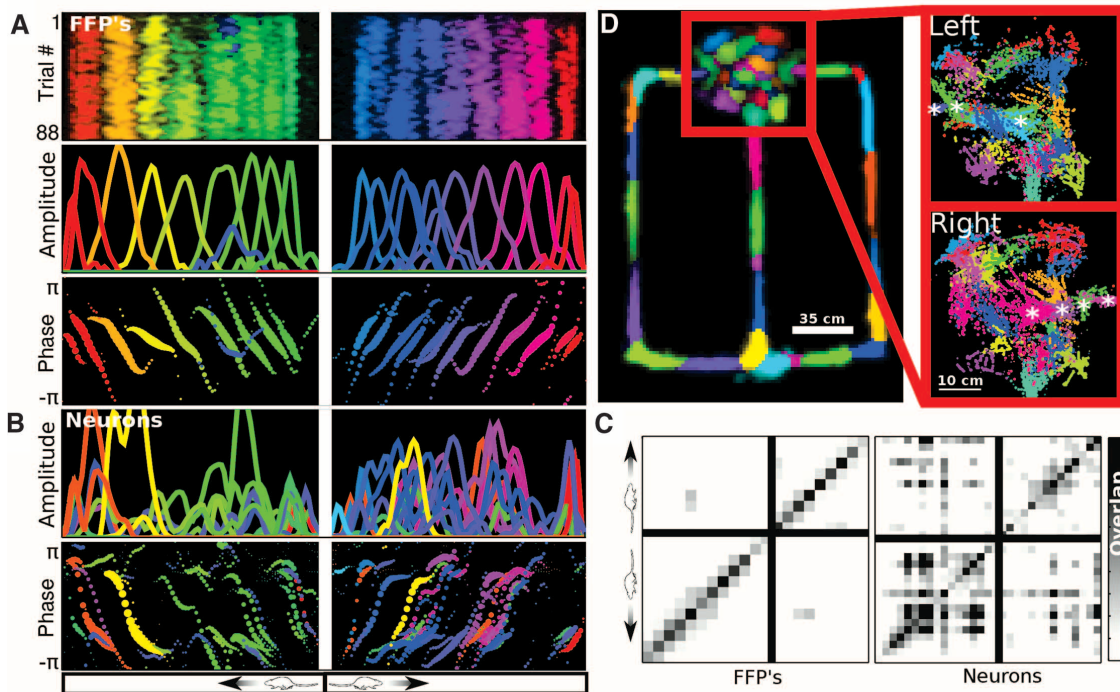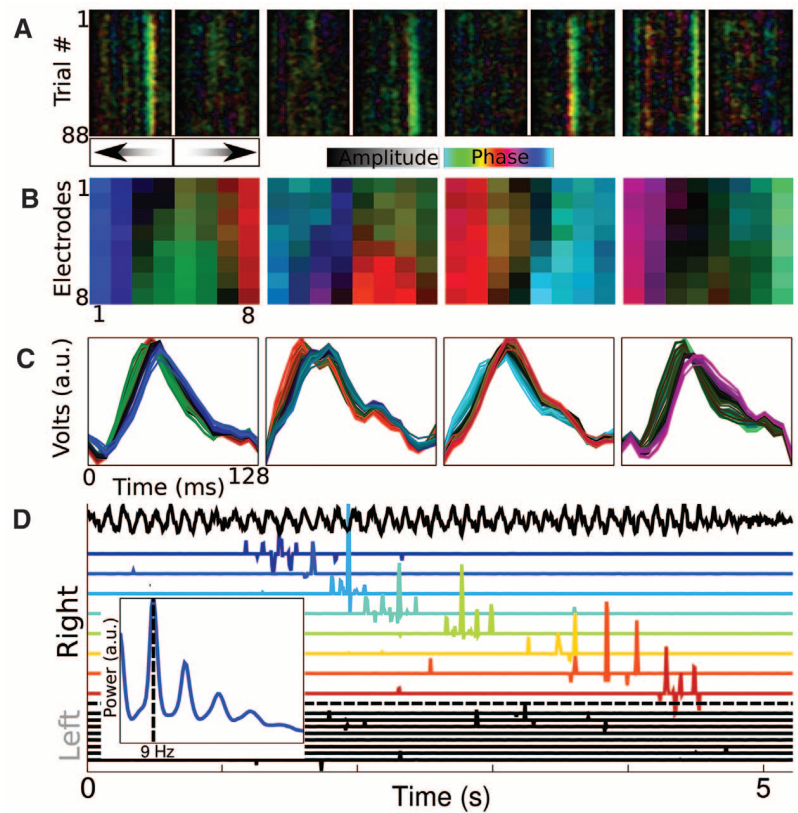

Fig. 4. Population properties of FFPs and neuronal spikes during a single session. (**A**) FFPs uniformly tile the length of the track. The spatial extent and spacing of different FFPs is largely homogeneous across the track (middle). FFPs exhibit phase precession with respect to PC1 (bottom). (**B**) Pyramidal cells have place fields that are more variable in extent and distribution. (**C**) The overlap of FFP activations is largely restricted to neighbors, unlike that for pyramidal cells [grayscale range of P(Overlap) = 0 to 0.1]. (**D**) Activation of FFPs in a T maze. Waiting area is enclosed in a red box. Right panels show close-up of activations in waiting area, separated by direction of entry. Asterisks mark activations that are entry-direction selective. Each point represents a time bin where FFP activation exceeds a threshold, its size indicating the magnitude of activation. In (A) and (B), place-field hues are assigned based on location of maximal activation; in (D), hues are assigned to distinguish neighbors. Data for (A), (B), and (C) are collected by a 64-electrode array; (D) was from 2- by 256-electrode arrays.

organized brain regions, this limitation is less hampering, because the electrode conveys the activity of similarly tuned neurons (*21*, *22*). In contrast, because place cells in the hippocampus are distributed without topographic ordering (*23*), the LFP measured at any single location exhibits only weak place-modulation (fig. S9). However, compressed sensing methods can recover sparse signals even from mixed and subsampled measurements (*15*). During movement, population activity in the hippocampus is largely determined by a single (i.e., highly sparse) cause: the rat's current position. Therefore, distributed messages can be discovered by unsupervised learning methods such as ICA (*14*). Our experimental and simulation results show that the ICA-derived FFPs exhibit several properties reminiscent of place cells: They have smooth, localized place fields, exhibit phase precession, and show considerable trial-by-trial variability (*24*). Building on earlier work [e.g., (*25*)], these findings show how large-scale recordings of LFP can help in understanding the organization of activity in other brain regions, as well as developing robust decoders for brain-computer interfaces.

References and Notes

1. M. A. Wilson, B. L. McNaughton, *Science* **261**, 1055–1058 (1993).
2. W. J. Freeman, *Clin. Neurophysiol.* **115**, 2077–2088 (2004).
3. G. Buzsáki, C. A. Anastassiou, C. Koch, *Nat. Rev. Neurosci.* **13**, 407–420 (2012).
4. S. Łęski, H. Lindén, T. Tetzlaff, K. H. Pettersen, G. T. Einevoll, *PLOS Comput. Biol.* **9**, e1003137 (2013).
5. N. K. Logothetis, *J. Neurosci.* **23**, 3963–3971 (2003).
6. E. R. John, *Science* **177**, 850–864 (1972).
7. J. O'Keefe, L. Nadel, *The Hippocampus as a Cognitive Map* (Clarendon Press, Oxford Univ. Press, Oxford and New York, 1978).
8. C. H. Vanderwolf, *Electroencephalogr. Clin. Neurophysiol.* **26**, 407–418 (1969).
9. G. Buzsáki, E. I. Moser, *Nat. Neurosci.* **16**, 130–138 (2013).
10. C. Geisler *et al.*, *Proc. Natl. Acad. Sci. U.S.A.* **107**, 7957–7962 (2010).
11. A. Berényi *et al.*, *J. Neurophysiol.* **111**, 1132–1149 (2014).
12. O. Jensen, J. E. Lisman, *J. Neurophysiol.* **83**, 2602–2609 (2000).
13. K. Zhang, I. Ginzburg, B. L. McNaughton, T. J. Sejnowski, *J. Neurophysiol.* **79**, 1017–1044 (1998).
14. C. Hillar, F. T. Sommer, When can dictionary learning uniquely recover sparse data from subsamples? (2011); http://arxiv.org/abs/1106.3616).
15. D. L. Donoho, *Inf. Theory IEEE Trans. On* **52**, 1289–1306 (2006).
16. A. Hyvärinen, E. Oja, *Neural Netw.* **13**, 411–430 (2000).
17. M. Novey, T. Adali, *Proc. IEEE Workshop Mach. Learn. Signal Process* (Arlington, VA, 6 to 8 September, 2006), pp. 79–84.
18. A. Khosrowshahi *et al.*, *Exploring the Statistical Structure of Large-Scale Neural Recordings Using a Sparse Coding Model* (Cosyne, Salt Lake City, UT, 2010).
19. J. O'Keefe, M. L. Recce, *Hippocampus* **3**, 317–330 (1993).
20. E. Pastalkova, V. Itskov, A. Amarasingham, G. Buzsáki, *Science* **321**, 1322–1327 (2008).
21. C. Mehring *et al.*, *Nat. Neurosci.* **6**, 1253–1254 (2003).
22. A. de Cheveigné, J.-M. Edeline, Q. Gaucher, B. Gourévitch, *J. Neurophysiol.* **109**, 261–272 (2013).
23. A. D. Redish *et al.*, *J. Neurosci.* **21**, RC134 (2001).
24. R. Schmidt *et al.*, *J. Neurosci.* **29**, 13232–13241 (2009).
25. W. J. Freeman, B. Baird, *Behav. Neurosci.* **101**, 393–408 (1987).
26. K. Mizuseki, A. Sirota, E. Pastalkova, K. Diba, G. Buzsaki, Multiple single unit recordings from different rat hippocampal and entorhinal regions while the animals were performing multiple behavioral tasks (2013); available at http://crcns.org/data-sets/hc/hc-3.

Vascular and Neurogenic Rejuvenation of the Aging Mouse Brain by Young Systemic Factors

Lida Katsimpardi,[1,2]* Nadia K. Litterman,[1,2] Pamela A. Schein,[1,2] Christine M. Miller,[1,2,3] Francesco S. Loffredo,[1,2,4] Gregory R. Wojtkiewicz,[5] John W. Chen,[5] Richard T. Lee,[1,2,4] Amy J. Wagers,[1,2,3] Lee L. Rubin[1,2]*

In the adult central nervous system, the vasculature of the neurogenic niche regulates neural stem cell behavior by providing circulating and secreted factors. Age-related decline of neurogenesis and cognitive function is associated with reduced blood flow and decreased numbers of neural stem cells. Therefore, restoring the functionality of the niche should counteract some of the negative effects of aging. We show that factors found in young blood induce vascular remodeling, culminating in increased neurogenesis and improved olfactory discrimination in aging mice. Further, we show that GDF11 alone can improve the cerebral vasculature and enhance neurogenesis. The identification of factors that slow the age-dependent deterioration of the neurogenic niche in mice may constitute the basis for new methods of treating age-related neurodegenerative and neurovascular diseases.

In the adult brain, neural stem cells reside in a three-dimensional (3D) heterogeneous niche, where they are in direct contact with blood vessels and the cerebrospinal fluid. The vasculature can influence neural stem cell proliferation and differentiation by providing a local source of signaling molecules secreted from endothelial cells (*1*) as well as by delivering systemic regulatory factors (*2*). The hormone prolactin (*3*), dietary restriction (*4*), and an exercise/enriched environment (*5*) positively modulate neurogenesis, whereas increased levels of glucocorticoids associated with stress have the opposite effect (*6*). In the aging niche, the vasculature deteriorates with a consequent reduction in blood flow (*7*), and the neurogenic potential of neural stem cells declines, leading to reduced neuroplasticity and cognition (*8–10*). Systemic factors can also affect these aging-associated events, either positively in which circulating monocytes enhance remyelina-

tion in aged mice (*11*, *12*) or negatively in which the accumulation of chemokines in old blood can reduce neurogenesis and cognition in young mice (*10*).

To test whether the age-related decline of the neurogenic niche can be restored by extrinsic young signals, we used a mouse heterochronic parabiosis model. Our experiments reveal a remodeling of the aged cerebral vasculature in response to young systemic factors, producing noticeably greater blood flow, as well as activation of subventricular zone (SVZ) neural stem cell proliferation and enhanced olfactory neurogenesis, leading to an improvement in olfactory function. Furthermore, we tested GDF11, a circulating transforming growth factor–β (TGF-β) family member that reverses cardiac hypertrophy in aged mice (*13*), and found that it can also stimulate vascular remodeling and increase neurogenesis in aging mice. Thus, we have observed that age-dependent remodeling of this niche is reversible by means of systemic intervention.

[1]Department of Stem Cell and Regenerative Biology, Harvard University, Cambridge, MA 02138, USA. [2]Harvard Stem Cell Institute, Cambridge, MA 02138, USA. [3]Howard Hughes Medical Institute, Joslin Diabetes Center and the Paul F. Glenn Laboratories for the Biological Mechanisms of Aging, Harvard Medical School, Boston, MA 02115, USA. [4]Cardiovascular Division, Department of Medicine, Brigham and Women's Hospital, Boston, MA 02115, USA. [5]Center for Systems Biology and Department of Radiology, Massachusetts General Hospital, Harvard Medical School, Boston, MA 02115, USA.

*Corresponding author. E-mail: lee_rubin@harvard.edu (L.L.R.); lida_katsimpardi@harvard.edu (L.K.)